AIAA JOURNAL
Vol. 36, No. 10, October 1998

Development of a Nearly Omnidirectional Velocity Measurement Pressure Probe

Othon K. Rediniotis* and Robert E. Kinser†
Texas A&M University, College Station, Texas 77843-3141

The development of a nearly omnidirectional pressure probe for three-velocity-component and pressure measurements is described, focusing on the techniques employed in probe fabrication, calibration, and frequency-response study. The probe tip is a sphere with 18 pressure ports properly distributed over the spherical surface. The device eliminates the velocity directionality limitations of current multihole probes and constitutes a rugged tool for use in complex three-dimensional flow mapping. An automated calibration system was used to generate a probe calibration database of approximately 10,000 individual probe orientations. Least-squares-based and neural-network-based calibration algorithms were developed. The reliability of the calibration procedures and algorithms is demonstrated first. Then probe utility is demonstrated in a flowfield with flow reversal, downstream of a backward-facing step. Last, a study of the probe frequency response is presented.

I. Introduction

THE design, evaluation, and optimization of complex aerodynamic geometries involve extensive wind-tunnel testing and/or computationally intensive numerical simulations. Even in the latter case, high-quality experimental wind-tunnel results with minimal, quantifiable errors are still necessary for code-validation purposes. Moreover, in aerodynamic testing facilities where large volumes of data need to be acquired in tight schedules, downtime due to poor instrumentation performance is highly undesirable. Such facilities include industrial testing wind tunnels, as well as high-productivity computational fluid dynamics code validation facilities.[1] In such environments, flow measurement techniques such as laser Doppler velocimetry and particle image velocimetry, although powerful, usually require painstaking efforts toward their successful usage. Costly components; complex setups; troublesome flow seeding requirements; lack of flexibility, ruggedness, and mobility; and ease of misalignment often render such techniques impractical. Moreover, in testing of complex three-dimensional geometries, accessibility of the entire flowfield around the model is an essential issue. When employing optical techniques, large sections of the flowfield are obstructed optically by the presence of the model. To access such regions, repositioning of the instrumentation setup is necessary, a time-consuming process with the associated potential pitfalls.

Multihole pressure probes[2–7] in many cases have provided the easiest-to-use and most cost-effective method for three-component flow velocity measurements in research and industry environments. However, even with expanded measurement capabilities of such instruments, the current pressure probe configurations and techniques have a limited range of velocity inclinations that they can measure. The velocity inclination is indicated as the cone angle θ in Fig. 1. Let $\theta_{\max}$ be the maximum cone angle that can be measured reliably by the probe. In other words, a probe with a $\theta_{\max}$ of 40 deg can accurately measure any velocity vector that is contained within a cone with its apex at the probe tip, its axis along the probe axis, and with an apex included angle of 80 deg (Fig. 1). Measurable cone angles as high as 75 deg are not uncommon for seven-hole probes.[7] Following this reasoning, an omnidirectional probe is a probe that has a cone angle of 180 deg (360 deg included angle); i.e., it can measure any velocity vector regardless of its orientation.

The present work describes the development of a nearly omnidirectional probe that can measure up to cone angles of 170 deg (340 deg included). Therefore, almost any velocity orientation is measurable by the probe. For brievity, the probe is referred to as the omniprobe. The remainder of this paper discusses the design and fabrication of the probe and its calibration for use in incompressible flows, presents validation of probe calibration, demonstrates probe operation in flowfields with flow reversal, and examines probe frequency response issues.

II. Probe Design and Fabrication

Multihole probes have, in many cases, consisted of several small-diameter tubes axisymmetrically arranged inside a larger tube with one end machined into a cone. The apex of the cone coincides with the central hole, which is surrounded by four or six equally spaced holes. These simple probes have the advantage of easy construction and small size; however, they have flow angularity limitations. The omniprobe presented here overcomes this limitation. The significantly larger number (18) of pressure ports employed, however, required a break from traditional five- and seven-hole probe design and construction. The symmetry of a sphere on which the ports are arranged lends itself to the realization of omnidirectionality. However, the simple straight-through plumbing that makes five- and seven-hole probes easy to construct is not possible here. A particular arrangement of 18 holes on a sphere was found to facilitate the fabrication process.

The basic structural features of the spherical probe head are illustrated in Fig. 2. The port arrangement on the spherical head is presented in a coordinate system that emphasizes the grouping of the 18 ports into six five-hole configurations (Fig. 2a; the sting is omitted). In the coordinate system of Fig. 2a the pressure ports are marked as black dots and are distributed as follows (in terms of their spherical coordinates):

Eight ports at $\theta = 90$ deg and $\phi = 0$, 45, 90, 135, 180, 225, 270, and 315 deg
Four ports at $\phi = 0$ deg and $\theta = 0$, 45, 135, and 180 deg
Two ports at $\phi = 180$ deg and $\theta = 45$ and 135 deg
Two ports at $\phi = 90$ deg and $\theta = 45$ and 135 deg
Two ports at $\phi = 270$ deg and $\theta = 45$ and 135 deg

The ports, when properly combined in six groups of five, as indicated in Fig. 2a, form a network of five-hole configurations (some ports are shared by two groups). Each one of these configurations operates as a five-hole probe. The central ports of these five-hole configurations are the ports located at the intersections of each one of the xyz coordinate axes and the surface of the sphere. As discussed in Sec. V, each one of the five-hole configurations can be calibrated to provide accurate measurement of any velocity vector within a cone angle of 60 deg, i.e., any velocity vector with $\theta_i \leq 60$ deg, where θ_i measures from the axis of the ith five-hole configuration ($i = 1 \ldots 6$). If, now, all six configurations and their measurement

---

Received July 16, 1997; revision received May 18, 1998; accepted for publication May 26, 1998. Copyright © 1998 by the American Institute of Aeronautics and Astronautics, Inc. All rights reserved.

*Assistant Professor, Aerospace Engineering Department. Member AIAA.

†Research Assistant, Aerospace Engineering Department.

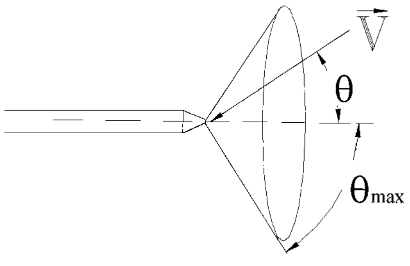

Fig. 1 Cone angle definition.

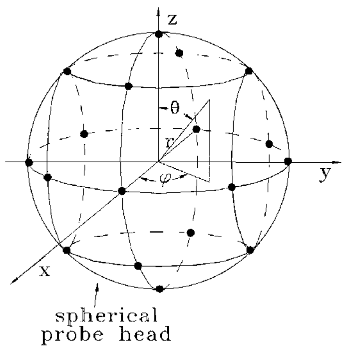

a) Port arrangement and grouping into six five-hole configurations

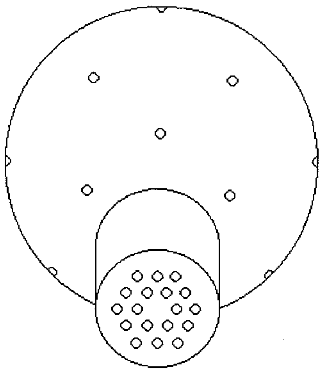

b) Probe head

Fig. 2 Probe structure schematics.

ranges are combined, almost any possible velocity vector can be measured accurately. The probe sting obviously interferes with the global symmetry of the spherical probe. However, its effect is minimized by having the sting intersect the sphere at the geometrical center of three adjacent five-hole configurations. The presence of the sting obviously affects the flowfield sensed by the adjacent five-hole configurations. As shown later, this effect is largely accounted for in the calibration process.

Another property of this geometry is that the holes align themselves with the sting in such a way as to allow hexagonal arrangement of the tubes inside the sting, which in turn minimizes the sting size. The internal plumbing of the sphere is significantly more complicated than that of five- or seven-hole probe designs. Precision machining of a brass sphere was used to drill the individual ports normal to the spherical surface. These holes then were intersected with 18 parallel holes drilled from the back of the sting. Figure 2b is a perspective schematic of the fabricated probe head, showing the drilled holes on the sphere and the base of the sting. Each of these holes is 0.010 in. in diameter. This dimension imposes, by geometry, a lower limit to the sting diameter and, implicitly, a lower limit to the sphere diameter. The result is a spherical probe head of 0.242 in. in diameter with a sting of 0.090 in. in diameter.

III. Pressure Measurement Hardware

Each one of the probe surface pressure ports needs to be connected through tubing to a pressure transducer. Therefore, 18 pressure transducers are required. Mechanical Scanivalve systems that utilize only one pressure transducer and mechanical scanning were not considered because of their slow pressure data acquisition rates, although, in theory, such a scanning system leads to slightly greater accuracy and could be used.[4] Instead, pressure data were acquired during probe calibration and use with a 32-transducer electronic pressure scanner (ESP) from PSI, Inc., with a pressure range of ±20 in. H_2O. The ESP pressure scanner was interfaced to a laboratory computer and was calibrated online. The small size of the ESP allowed us to position it very close to the end of the probe sting (ESP unit was at a distance of 12 in. from the probe tip), thus minimizing the length of the pressure tubing required. This, in turn, resulted in an increase of the frequency response of the entire pneumatic system. As mentioned earlier, the probe size was kept small for minimum possible intrusiveness and maximum possible spatial resolution, yet large enough to allow for limited temporal resolution capabilities. Obviously, it is the geometry of the plumbing/tubing assembly from the hole on the surface of the probe to the pressure transducer that determines the temporal resolution, not the size of the probe tip. However, the size of the tubing assembly relates to the size of the spherical tip. Because all of the tubing has to go through the sting, the larger the tubing, the larger the sting, and the larger the sting, the larger the sphere size, if the dimensional proportions of sting-sphere are to be kept the same. Otherwise, if the sting size is allowed to increase while the sphere size is kept the same, sting interference effects become larger and in turn limit the measurable angular range of the probe.

IV. Calibration Setup

The spherical probe was calibrated with the apparatus described in this section for the entire angularity range, for incompressible flow. A schematic of the probe calibration assembly is shown in Fig. 3. The calibration apparatus can be employed in either of two test facilities, a 3 × 4 ft or a 2 × 3 ft wind tunnel. The dual-axis, stepper-motor assembly is fully computer controlled and can vary the cone and roll angles (θ, ϕ) within the ranges (0 deg, 180 deg) and (−180 deg, 180 deg), respectively, thus covering the entire 4π solid angle of the calibration domain. However, in the present work the cone angle was varied between 0 and 170 deg because, for higher cone angles, the probe head ended up in the wake of the roll stepper motor. The positioning resolution for the calibration assembly is 0.32 deg in cone and 0.9 deg in roll, allowing for a maximum of about 220,000 calibration data points (individual angular orientations of the probe) over the calibration domain. However, a calibration database of about 10,000 points proved sufficient. More specifically, the cone angle θ was varied from 0 deg to about 170 deg, every 2.24 deg; i.e., there was a total of 77 calibration cone angles. For each one of these cone angles, the roll angle ϕ was varied from 0 to 360 deg, every 2.7 deg; i.e., there was a total of 133 individual calibration roll angles. Therefore, there was a total of $77 \times 133 = 10{,}241$ calibration angles.

The stepper-motor assemblies position the probe according to a user-defined array of probe orientations (θ_i, ϕ_i), $i = 1, \ldots, m$. For each orientation the data-acquisition system collects 19 pressures referenced to the tunnel static pressure, 18 from the probe and 1 from the stagnation port of a pitot tube positioned in the tunnel freestream. For each calibration point, 600 pressure readings were sampled per pressure port, over a period of 6 s. Calibration and data acquisition were performed in the 3 × 4 ft Aerospace Engineering Wind Tunnel. This is a closed-circuit tunnel with a test section equipped with a

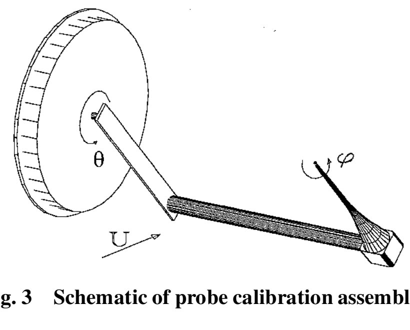

Fig. 3 Schematic of probe calibration assembly.

breather so that the static freestream pressure is equal to the control-room pressure. The clear Plexiglas® test section is 4 ft wide, 3 ft tall, and 6 ft long. The contraction ratio is 9 to 1. The maximum speed achieved in the tunnel is about 150 ft/s with a freestream turbulence less than 0.16%. To avoid temperature variations over time, there is an active cooling system to keep the freestream temperature at about 60°F during testing.

The probe was calibrated at a single Reynolds number $Re = 9.1 \times 10^3$, based on probe head diameter and freestream velocity. For incompressible flows, calibration dependence on Reynolds number is minimized by the fact that the flow separation over the spherical probe head is laminar. Noting that, typically, transition to turbulent separation occurs on spheres at a diameter-based Reynolds number of 3×10^5, it can be seen that a 0.242-in.-diam probe head experiences laminar separation for the entire range of incompressible conditions. Following the calibration process, test data points not coinciding with the calibration points also were collected for calibration validation, as discussed in Sec. VII.

V. Calibration Theory

The probe-associated coordinate systems and the angle definitions are illustrated in Fig. 4. $\boldsymbol{V}$ is the velocity vector incident on the probe head. Note that there is a one-to-one correspondence between the pitch and yaw (p, y) and the cone and roll (θ, ϕ) pairs, as defined by the following relations:

$$\sin\theta\cos\phi = \cos p \sin y, \qquad \sin\theta\sin\phi = \sin p \tag{1}$$

Each one of the five-hole groups then can be calibrated to provide accurate measurement of any velocity vector within a cone angle of 60 deg with respect to the axis of that particular five-hole configuration. If all six five-hole configurations and their measurement ranges are combined, any possible velocity vector can be measured accurately. From the preceding, it is obvious that two types of coordinate systems are necessary for the calculation of the flow parameters. The first coordinate system, which is referred to as the global coordinate system, is such that its X axis is aligned with the probe sting axis (Fig. 4). The second type of coordinate system is referred to as a local coordinate system and is associated with a particular five-hole configuration. Therefore, there are six such local coordinate systems, one for each five-hole group. Each local coordinate system is such that its x axis goes through the central hole of the particular five-hole configuration and is perpendicular to the spherical surface; i.e., it runs along a sphere radius. Figure 4 also could represent a local coordinate system aligned with a particular five-hole group. In this sense we must differentiate between global and local flow angles p, y, θ, ϕ, as well as global and local velocity components. Of course, the local parameters are simply variables used in the intermediate steps of the data reduction process. The final answers are always in global coordinates.

The flow over a five-hole probe typically can be divided into one low-angle sector and four high-angle sectors (Fig. 5). Each sector is identified by a number indicating the hole that senses the highest pressure for all of the possible velocity orientations in that sector. For low-angle flow, the highest pressure is registered by hole 1 (central hole); for high-angle flows, the highest pressure occurs in one of the peripheral holes 2–5. At every measurement location in a flow-mapping experiment, the velocity vector can be characterized fully by four variables. In the low-angle regime the four variables are pitch angle p, yaw angle y, total pressure coefficient A_t, and static pressure coefficient A_s. Once these variables are known, the total and static pressures P_t and P_s are calculated from A_t and A_s, respectively, and the velocity magnitude is calculated from P_t and P_s. Similarly, in the high-angle regime the four variables are cone angle θ, roll angle ϕ, A_t, and A_s. For either regime, high or low angle, these variables need to be determined as functions of the five measured pressures or, equivalently, the two nondimensional pressure coefficients formed from these pressures: B_p, B_y for low-angle flow and B_c, B_r for high-angle flow. All variables are with respect to the local coordinate system corresponding to the five-hole configuration of interest and are defined as follows:

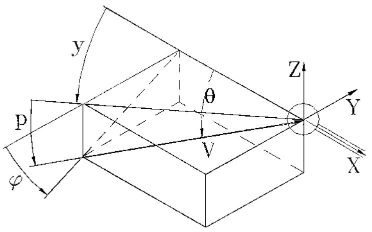

Fig. 4 Spherical probe coordinate systems (angle symbols: cone θ, roll ϕ, pitch p, yaw y).

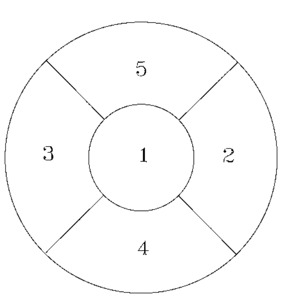

Fig. 5 Five-hole measurement domain divided into five sectors, each centered on an individual pressure port, labeled 1–5.

Low-angle regime (sector 1).

Independent (input) variables

$$B_p = \frac{P_4 - P_5}{P_1 - \bar{P}}, \qquad B_y = \frac{P_2 - P_3}{P_1 - \bar{P}} \tag{2a}$$

Dependent (output) variables

$$A_t = \frac{P_1 - P_t}{P_1 - \bar{P}}, \qquad A_s = \frac{P_1 - P_s}{P_1 - \bar{P}}$$
$$\text{pitch angle } p, \qquad \text{yaw angle } y \tag{2b}$$

where

$$\bar{P} = \frac{P_2 + P_3 + P_4 + P_5}{4}$$

High-angle regimes (sectors 2–5).

Independent (input) variables

$$B_c = \frac{P_i - P_1}{P_i - \bar{P}}, \qquad B_r = \frac{P_i^+ - P_i^-}{P_i - \bar{P}} \tag{3a}$$

Dependent (output) variables

$$A_t = \frac{P_i - P_t}{P_i - \bar{P}}, \qquad A_s = \frac{P_i - P_s}{P_i - \bar{P}}$$
$$\text{cone angle } \theta, \qquad \text{roll angle } \phi \tag{3b}$$

where

$$\bar{P} = \frac{P_i^+ + P_i^-}{2}$$

P_i is the highest detected pressure that occurs at the ith port. Use of the superscripts plus and minus facilitates conciseness in the notation. In the high-angle regimes (2–5) the definition of the pressure coefficients (B_c, B_r, A_t, A_s) depends on which one of the high-angle sectors senses the maximum pressure. The use of the plus and minus notation enables a unified definition of these pressure coefficients. If i is the peripheral port that senses the maximum pressure, then plus indicates the peripheral port adjacent to port i and in the clockwise direction from port i, when looking into the probe tip. Similarly, minus indicates the peripheral port in the counterclockwise direction.

During probe calibration, the calibration data are acquired and recorded in the global coordinate system, i.e., in terms of global cone and roll angles (Fig. 4). The data then are transformed to the local coordinate systems for the calibration of each five-hole configuration. As mentioned earlier, each five-hole configuration has a local cone and roll coordinate system as well as a local pitch and yaw coordinate system associated with it. To resolve the u, v, w velocity components from the 18-hole probe pressure data, two schemes have been developed: a local least-squares (LLS) interpolation algorithm and a neural-network-based algorithm. Both algorithms have been integrated in a single software package that, for a specific probe, automatically selects which approach will be used to reduce the pressure data to velocities. This selection process is based on performance data obtained from the calibration validation process described later. For the present work the code was hard-wired to use the LLS interpolation algorithm. For detailed descriptions of the two methods, the reader is referred to Refs. 8 and 9.

VI. Uncertainty Analysis

The uncertainty analysis presented here is based on the techniques discussed by Moffat,[10] and their application to the omniprobe problem follows the procedures discussed by Zilliac.[4] First, the uncertainty of the pressure measurement hardware is estimated. The pressure scanner used was calibrated during calibration of the probe, online, every hour. A five-point calibration was performed that accounted for transducer nonlinearities and thermal drifts. The reference manometer used for calibration had an uncertainty of 0.005 torr for the range of pressures used here (±5 torr). The preceding combination, along with a one-count A/D conversion uncertainty of the 16-bit A/D board, yielded a pressure measurement worst-case error of 0.015 torr or 0.009 in. H_2O. Errors in angular positioning were negligible. The resolution of the cone and roll positioning stepper motors (0.32 and 0.9 deg) should not be confused with their positioning precision, which is on the order of arc seconds. Bias errors due to probe sting deflection were also negligible at the speeds of calibration and for the specific structural design of the sting.

The uncertainty in the evaluation of the pressure coefficients B_p, B_y, B_c, B_r, A_t, and A_s was calculated using their definition formulas (2a) through (3b) and constant-odds combination[10] given by

$$\delta C_p = \sqrt{\sum_i \left(\frac{\partial C_p}{\partial P_i} \delta P_i \right)^2} \tag{4}$$

where C_p is any of the pressure coefficients and δP_i is the uncertainty in the measurement of pressure P_i. For example, the uncertainty in the evaluation of B_p is given by

$$\delta B_p = \left(\frac{1}{4P_1 - P_2 - P_3 - P_4 - P_5} \right)^2 \{256(P_4 - P_5)^2(\delta P_1)^2 + 16(P_4 - P_5)^2[(\delta P_2)^2 + (\delta P_3)^2] + 16(4P_1 - P_2 - P_3 - 2P_5)^2 \times (\delta P_4)^2 + 16(4P_1 - P_2 - P_3 - 2P_4)^2(\delta P_5)^2\}^{\frac{1}{2}} \tag{5}$$

Subsequently, and to see how the uncertainty in the calculation of the pressure coefficients propagates through the LLS fitting algorithm, a jitter approach[10] was followed. The estimates of the δP_i were obtained from a Gaussian distribution with zero mean and a standard deviation of 0.005 torr. This was chosen so that the worst-case error in pressure measurement, i.e., 0.015 torr, corresponds to three standard deviations from the mean, which in turn corresponds to a 99.5% probability that the pressure measurement error is smaller than or equal to 0.015 torr. The preceding allowed the estimation of uncertainty in B_p (or B_c), B_y (or B_r), A_t, and A_s for every calibration and test point, through Eq. (4). The obtained δB_p (or δB_c), δB_y (or δB_r), δA_t, and δA_s were used to perturb the original values of these coefficients for the calibration points, and the perturbed values subsequently were used by the LLS algorithm to reduce the test data that also were perturbed in the manner explained earlier. The predictions obtained in this process were compared to those obtained from the unperturbed calibration and test points, and the standard deviation of the differences between these two yielded estimates for the overall uncertainty. The uncertainty results (pitch and yaw angles in the low-angle regimes were converted to the equivalent cone and roll angles) are cone angle, 0.14 deg; roll angle, 0.2 deg; and velocity magnitude, 0.6%.

The contribution of the LLS fitting technique alone to the overall uncertainty also was evaluated. The calibration fitting procedure is, in many conventional probe-data-reduction algorithms, found to be one of the greatest sources of error. Using a global surface to fit all or large sectors of the calibration data compromises the surface's ability to capture local features of the calibration surface, often caused by fabrication imperfections of the probe tip surface. The present LLS approach is substantially more accurate, as intuitively suspected but also as proven by the uncertainty analysis discussed next. The uncertainty evaluation was performed on an analytical surface that captured the local characteristics (slope, curvature, etc.) of an actual probe calibration surface. Such model surfaces were generated from sets of calibration data points using TableCurve 3D. The uncertainty of our fitting technique then was evaluated on these model surfaces by calculating the error between the LLS prediction and the model surface for several points on the surface and then calculating the standard deviation of these errors. This process was repeated for different regions of the calibration map (low- and high-angle regions) and for all four calibration variables. The estimated uncertainties were no more than 0.01 deg in the angles and 0.05% in the velocity magnitude.

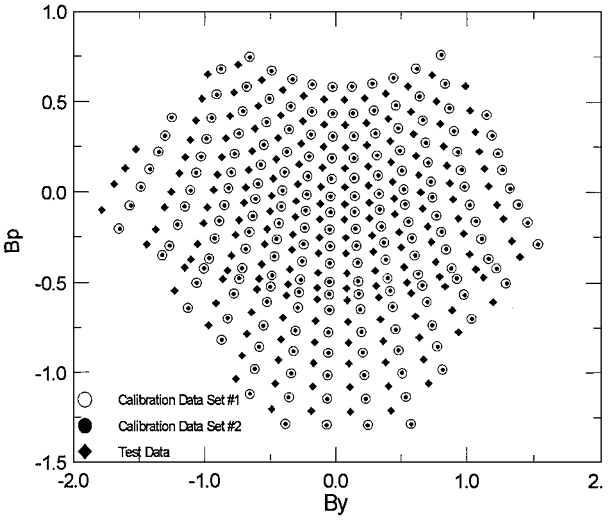

Fig. 6 Two calibration data sets, collected at two different times. Overlapping of calibration sets indicates good repeatability of the calibration data-acquisition process. A typical test data set also is presented.

Moreover, to establish confidence in the repeatability of the calibration data collection process and hardware, the same set of calibration data, for specific five-hole configurations, was collected several times, at different days and different times of the day. All data sets were taken at a freestream velocity of 72.5 ft/s. As an example of the typically achieved repeatability, two of these calibration sets are presented in Fig. 6 for the low-angle sector in the $B_y - B_p$ plane. Very good repeatability can be observed. In Fig. 6, we also present a sample of the test data collected for calibration validation purposes. As seen there, these data intentionally do not coincide with the calibration data.

VII. Calibration Validation

Figures 7–10 illustrate the typical performance of our calibration process. Emphasis is placed on the more challenging case of high-angle sectors. Test data points were used to generate the plots. In acquiring these test data points, the probe was positioned by the calibration rig to specified orientations angles (with respect to the freestream). These angles are referred to as the exact or actual angles. None of these test orientations coincided with any of the probe calibration orientations. At each one of these test orientations, the 18 probe pressures and the freestream dynamic pressure were sampled. The freestream dynamic pressure yielded the exact or actual velocity magnitude. The 18 probe pressures were fed into the probe calibration routines, which in turn produced predicted values for the probe orientation angles and the velocity magnitude. The comparison of these predicted values to the exact or actual values is presented in Figs. 7–10. Figures 7 and 8 present calibration performance for the cone and roll angles of a high-angle sector of a specific five-hole configuration, and Fig. 9 presents the predictions,

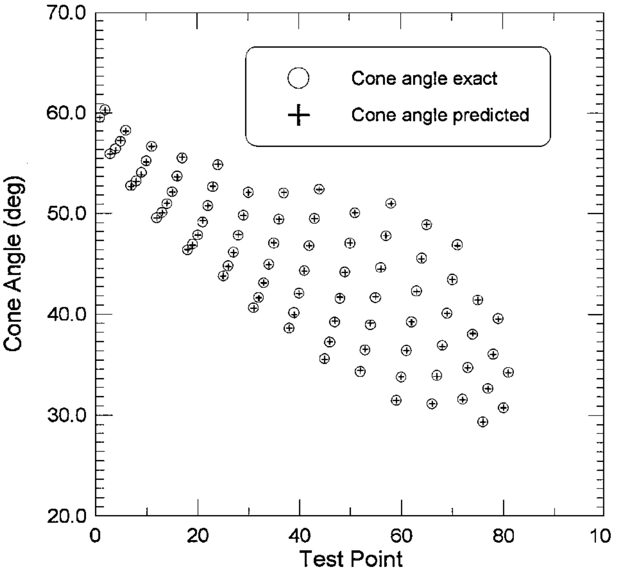

Fig. 7 Cone-angle prediction for a high-angle sector.

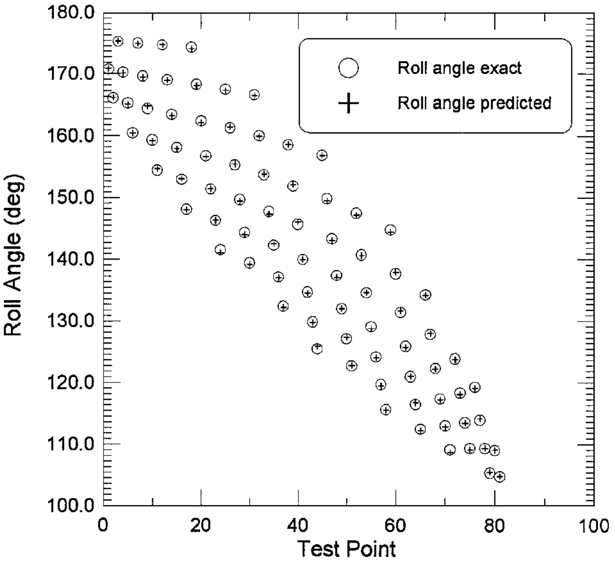

Fig. 8 Roll-angle prediction for a high-angle sector.

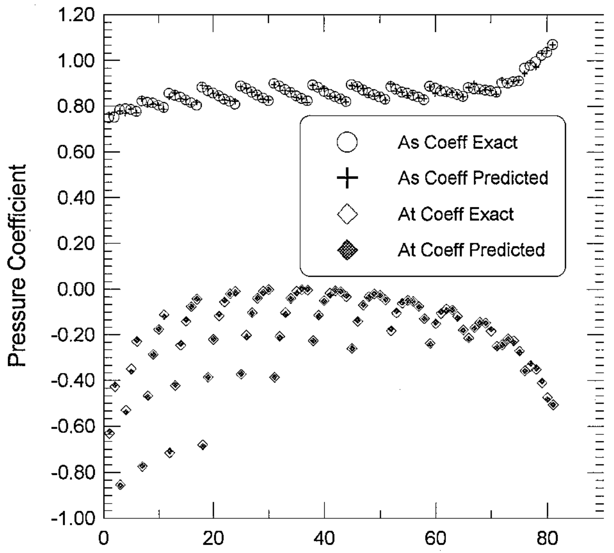

Fig. 9 Prediction of total and static pressure coefficients A_t and A_s, respectively, for a high-angle sector.

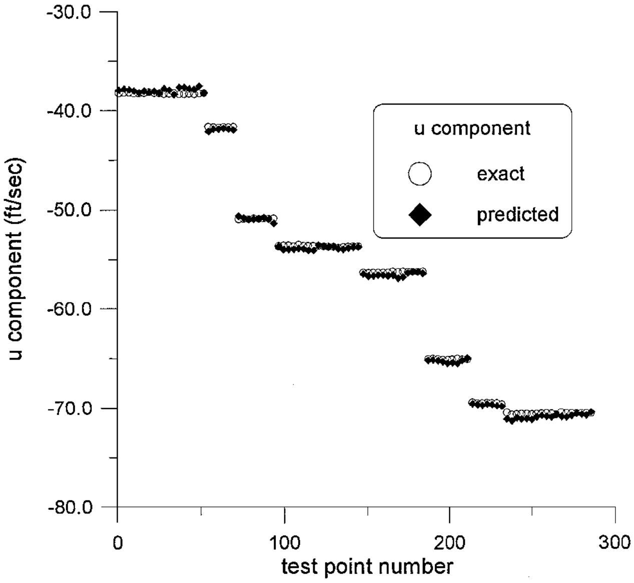

Fig. 10 Prediction of axial velocity component for reversed-flow conditions.

for the same high-angle sector, of the pressure coefficients A_t and A_s, which are directly related to the velocity magnitude. As the figures indicate, the prediction accuracy is very good. The cone-angle θ prediction has a maximum absolute error of 0.25 deg, a mean absolute error of 0.1 deg, and a standard deviation of 0.09 deg. The roll-angle ϕ prediction has a maximum absolute error of 0.5 deg, a mean absolute error of 0.21 deg, and a standard deviation of 0.18 deg. Excellent agreement also can be observed in the prediction of the total and static pressure coefficients A_t and A_s. These resulted in a velocity magnitude maximum absolute error of 1.5 ft/s, a mean absolute error of 0.52 ft/s, and a standard deviation of 0.4 ft/s. All of these error levels are within those predicted by the uncertainty analysis of Sec. VI. Low-angle sector data (p, y, A_t, and A_s) are predicted with accuracies higher than those quoted earlier for high-angle sectors.

Figure 10 illustrates the nearly omnidirectional measurement capability of the probe and the fact that sting interference is accounted for largely by the calibration process. The freestream and therefore the velocity magnitude that the probe is experiencing is 72.5 ft/s. Noting from Fig. 10 that u velocity components (component along the X axis of the probe, as shown in Fig. 4) as high as -71 ft/s are predicted accurately, it can be concluded that flow angularities as high as 170 deg in the cone can be resolved accurately.

VIII. Flow Survey Downstream of a Backward-Facing Step

A backward-facing step was constructed in the test section of the 3 × 4 ft wind tunnel. The step height was $H = 5.7$ in. and spanned the entire tunnel width. A flow survey downstream of the step was conducted with the 18-hole probe along a plane parallel to the freestream and perpendicular to the tunnel floor. Data were taken on a 85 (streamwise) × 14 (vertical) point orthogonal grid with a 0.5-in. spacing in both directions. The freestream velocity was 110 ft/s, corresponding to a Reynolds number, based on the step height, of 0.32×10^6. To avoid errors introduced by probe-wall interference, no data were obtained closer than 1 in. to the face of the step and 0.5 in. to the tunnel floor. At each measurement point, data were acquired and averaged for 10 s at a sampling rate of 500 Hz.

Figure 11 presents an in-plane velocity vector plot downstream of the step. Both axes have been nondimensionalized with the step height and the velocity vectors by the freestream velocity. Qualitatively, the probe has captured the reversed-flow region. Quantitatively, two tests were performed to assess probe measurement performance. Because the mean flow is two dimensional, a zero out-of-plane velocity component (perpendicular to the page) should be expected. The out-of-plane component was monitored at each

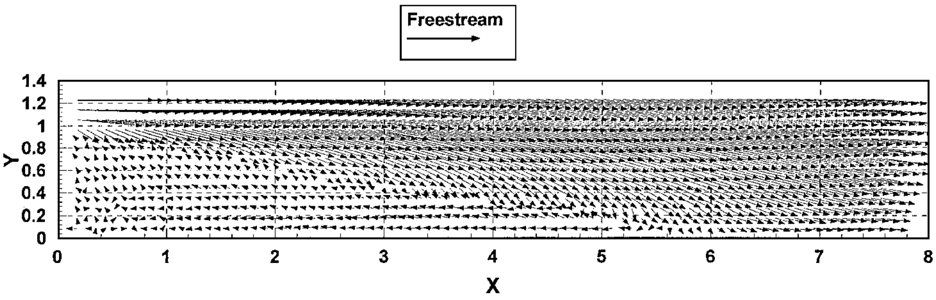

Fig. 11 Velocity vector plot downstream of a backward-facing step.

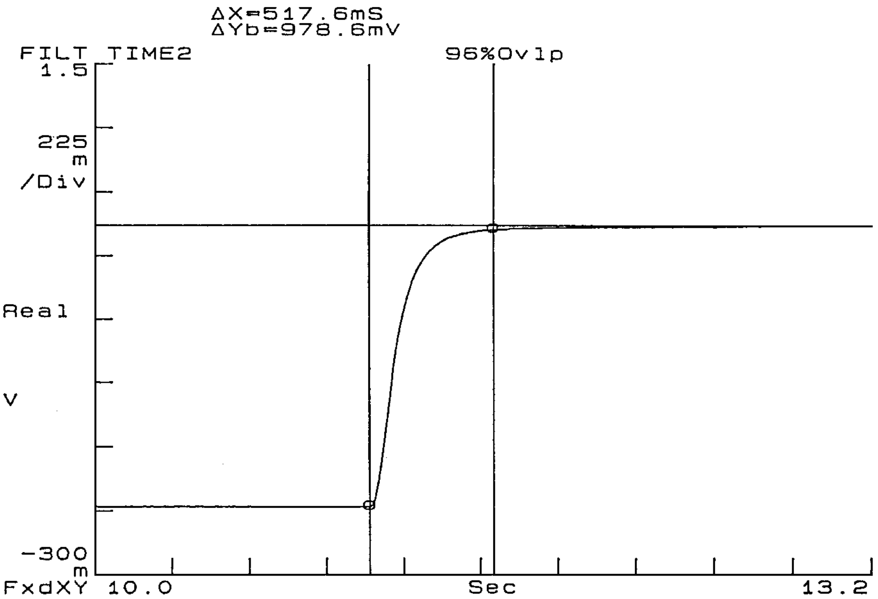

Fig. 12 Pressure tubing response for a typical probe tubing assembly (0.005-in.-i.d., 3-in.-long tube section plus 0.01-in.-i.d., 9-in.-long tube section).

measurement point and was found to be within ±1.5 ft/s, which is within the measurement accuracy of the device. Also, surface oil flow visualization was performed on the tunnel floor, to identify the reattachment line. Both techniques (probe and flow visualization) yielded a bubble size of 5.6 (step heights), to within 0.08 step heights of each other.

IX. Frequency Response Test

A test to assess the frequency response characteristics of the pressure tubing involved in the probe fabrication also was conducted. In a point-by-point, flow-mapping experiment, this information gives an idea on what the minimum wait time should be, i.e., the time that the probe would have to wait, after it moves to a new point, before the pressure data-acquisition process can begin. This time is required for the pressure sensed by the pressure transducers to equalize to the actual pressure at the tip of the probe. This time is important because it strongly affects the total time needed to complete a certain flow survey. The propagation of a pressure step of approximately 1 in. H_2O through a tubing configuration representative of the present probe was studied experimentally. This configuration is an assembly of two tubing sections: a 3-in.-long, 0.005-in.-i.d. section and a 9-in.-long, 0.01-in.-i.d. section. The pressure step is applied at one end of the tubing configuration. The output of a high-frequency-response Validyne pressure transducer (flat response up to 10 kHz) positioned at the other end, is recorded. The response time record is presented in Fig. 12. The ΔX value at the top of the plot is the pressure rise time at the pressure transducer end, from the initial pressure value to 99% of the final steady-state value. In this case, this time is approximately 0.5 s, which is a very acceptable wait time per point in a flow-mapping experiment.

X. Summary and Conclusions

A novel flowfield velocity and pressure measurement sensor with nearly omnidirectional velocity measurement capabilities has been developed. The probe's main element is an 18-pressure-port spherical head, 0.242 in. in diameter. The 18 pressure ports are distributed on the spherical surface so that they form a network of six five-hole configurations. By calibrating each one of these configurations and by combining their measurement domains, any velocity direction within a cone angle of 170 deg can be resolved by the omniprobe. An automated calibration system was used to generate a probe calibration database of approximately 10,000 points. An LLS-based calibration algorithm was developed with very good prediction accuracy: maximum absolute error of 0.5 deg and mean absolute error of 0.21 deg in angle prediction; maximum absolute error of 1.5 ft/s (out of 72.5 ft/s) and mean absolute error of 0.52 ft/s in velocity magnitude prediction. A detailed uncertainty analysis of the probe calibration processes was presented. Probe use in reversed-flow environments was demonstrated via measurements downstream of a backward-facing step. Partial quantitative validation of probe measurement accuracy was achieved: Bubble size and out-of-plane velocity component were measured accurately. Finally, a test of the probe frequency response was presented and revealed, for the specific probe, wait times of 0.5 s, which is very reasonable for point-by-point flow surveys.

References

[1] Sellers, W. L., and Kjelgaard, S. O., "The Basic Aerodynamics Research Tunnel—A Facility Dedicated to Code Validation," AIAA Paper 88-1997, May 1988.

[2] Chue, S. H., "Pressure Probes for Fluid Measurement," *Progress in Aerospace Sciences*, Vol. 16, No. 2, 1975, pp. 147–223.

[3] Gallington, R. W., "Measurement of Very Large Flow Angles with Non-Nulling Seven-Hole Probes," USAFA-TR-80-17, U.S. Air Force Academy, CO, Oct. 1980.

[4] Zilliac, G. G., "Modeling, Calibration, and Error Analysis of Seven-Hole Pressure Probes," *Experiments in Fluids*, Vol. 14, No. 1/2, 1993, pp. 104–120.

[5] Kjelgaard, S. O., "Theoretical Derivation and Calibration Technique of a Hemispherical-Tipped Five-Hole Probe," NASA TM-4047, 1988.

[6] Everett, K. N., Gerner, A. A., and Durston, D. A., "Seven-Hole Cone Probes for High Angle Flow Measurement: Theory and Calibration," *AIAA Journal*, Vol. 21, No. 7, 1983, pp. 992–998.

[7] Rediniotis, O. K., Hoang, N. T., and Telionis, D. P., "The Seven-Hole Probe: Its Calibration and Use," *Forum on Instructional Fluid Dynamics Experiments*, Vol. 152, edited by R. S. Budwig, J. F. Foss, and D. E. Stock, American Society of Mechanical Engineers, New York, 1993, pp. 21–26.

[8] Kinser, E., and Rediniotis, O. K., "Development of a Nearly-Omni-Directional, Three-Component Velocity Measurement Pressure Probe," AIAA Paper 96-0037, Jan. 1996.

[9] Kinser, E., Furey, D. A., and Rediniotis, O. K., "Calibration Neural Network for a Novel Omni-Directional Velocity Probe—PROBENET," *Proceedings of the ASME Fluids Engineering Division*, FED-Vol 242, American Society of Mechanical Engineers, New York, 1996, pp. 9–16.

[10] Moffat, R. J., "Contributions to the Theory of Single-Sample Uncertainty Analysis," *Journal of Fluids Engineering*, Vol. 104, June 1982, pp. 250–258.

G. Laufer
Associate Editor